

## Computational discovery of two-dimensional copper chalcogenides CuX (X = S, Se, Te)

Somayeh Faraji <sup>1,\*</sup>, Busheng Wang,<sup>1</sup> Hubert Okadome Valencia <sup>2</sup>, and Gilles Frapper <sup>1,†</sup>

<sup>1</sup>Applied Quantum Chemistry Group, E4 Team, IC2MP UMR 7285,

Université de Poitiers - CNRS, 4, Rue Michel Brunet TSA 51106 - 86073 Poitiers Cedex 9, France

<sup>2</sup>Department of Material Physics, Nagoya University Furo-cho, Chikusa-ku, Nagoya 464-8603, Japan



(Received 10 September 2021; revised 28 November 2021; accepted 8 December 2021; published 28 December 2021)

We investigate the energy landscape of 2D CuS, CuSe, and CuTe compounds using a global evolutionary algorithm in combination with density functional theory. Four low-lying energy Cu<sub>2</sub>X<sub>2</sub> (X=S, Se, Te) slabs with  $P\bar{3}m1$ ,  $P4/mmm$ ,  $P4/nmm$ , and  $Pm\bar{m}n$  symmetries have been identified on their respective potential energy surfaces. Three structures present tetrahedral CuX<sub>4</sub> motifs which pave the 2D slabs, while the latter is based on shared Cu<sub>4</sub>X<sub>2</sub> octahedra. The viability of each phase was examined by looking at dynamical, thermodynamic, and thermal stability criteria. We find that 2D copper monosulfide crystallizes in the  $P\bar{3}m1$  phase, reminiscent of the covalent slab found in the CaAl<sub>2</sub>Si<sub>2</sub> prototype. Two polymorphs of 2D copper selenide with symmetries  $P\bar{3}m1$  and  $P4/mmm$  are close in energy. The latter Cu<sub>2</sub>Se<sub>2</sub> slab is made of fused Cu<sub>4</sub>Se<sub>2</sub> square bipyramids with electronegative Se atoms in apical positions. Finally, the ground-state 2D CuTe has a  $Pm\bar{m}n$  space group containing distorted CuTe<sub>4</sub> tetrahedra with some Te–Te bonding. The electronic and bond analyses show that all of these predicted 2D CuX phases are metallic with ionocovalent bonds.

DOI: [10.1103/PhysRevMaterials.5.124007](https://doi.org/10.1103/PhysRevMaterials.5.124007)

### I. INTRODUCTION

Two-dimensional (2D) materials present a class of materials with physics which have attracted significant interest in recent years, particularly since the discovery of graphene as a room-temperature 2D material [1]. Such 2D materials exhibit a wide range of extraordinary optical, mechanical, and electronic properties which are markedly different from their bulk counterparts. Owing to such properties, they have attracted the interest of many experimental and theoretical researchers to keep searching for novel 2D materials and understand their specific physical and chemical properties. While the focus of most of the initial research has been concentrated on 2D semiconductors [2], growing interest has been shown to metallic 2D materials, especially transition-metal monochalcogenides  $MX$  ( $M$  = transition metals like Cu, Fe, Pb, etc.;  $X$ =S, Se, Te) [3–5].

Binary copper chalcogenides CuX ( $X$  = S, Se, and Te) are potential materials with applications in photothermal therapy [6], batteries [7–9], and room-temperature sensors [10]. Copper sulfide nanocrystals have received special attention due to their unique optoelectronic properties [11]. Among them, CuS, known as covellite, is one of the most studied copper sulfides due to its large ion diffusion and adsorption band gap. It is, therefore, a good candidate for technological applications such as ammonia gas sensors [10], anticancer drugs [12], catalysts [9,13], glucose biosensors [14], and electrode materials for rechargeable Li-ion [11,15] or Mg-based [16] batteries. The copper-selenide system presents many phases

with potential applications for photothermal therapy [6], thermoelectric materials [17], or electrodes for supercapacitors [18]. Finally, the copper-telluride system is viewed as the most complex copper chalcogenide, owing to its several non-identical polymorphs for different Cu:Te ratios [19–21]. Its large thermoelectric power has attracted the interest of many researchers [22,23]. It can also be viewed as a quasi-one-dimensional charge density wave system [24], which is an intriguing fundamental phenomenon [25].

In addition to the studies briefly introduced above on bulk CuX materials, their low-dimensional structures have also drawn a lot of attention. In 2012, a single-crystal nanosheet of CuS with a thickness of 3.2 nm was fabricated [11] and used for rechargeable magnesium batteries [16]. Recently, a computational work based on density functional theory (DFT) calculations has demonstrated that monolayer graphenelike structure CuS was unstable and the three-layered CuS (3L CuS) with a thickness of 0.773 nm was predicted to be intrinsically stable [26]. In addition, a CuS structure with flowerlike microspheres was synthesized [27]. It was shown that its loose shell was constructed from a graphenelike CuS nanosheet. To our knowledge, the 3L CuS is therefore proposed to be the thinnest stable freestanding CuS nanosheet with covellite stoichiometry. The structural, optical, and electronic properties of thin films of CuSe were also investigated [28]. The fabrication of a monolayer of CuSe grown on a Cu substrate was reported in 2017 [29]. It presents periodic patterns of triangular nanopores with uniform size and was reported as a honeycomb lattice of CuSe layers. A similar 1D moiré pattern of planar CuSe monolayers was then synthesized [30]. Then, it was shown that there is a strong electrical anisotropy and current-voltage curves along the zigzag and armchair directions of this graphenelike structure [31]. Thin films of

\*Corresponding author: [sfaraji86@gmail.com](mailto:sfaraji86@gmail.com)

†Corresponding author: [gilles.frapper@univ-poitiers.fr](mailto:gilles.frapper@univ-poitiers.fr)

copper telluride have been experimentally synthesized by many groups [32,33] and are used as a back contact for CdTe-based solar cells [34]. The latter structure was characterized by x-ray diffraction (XRD) as a polycrystalline structure, with preferred (101), (112), and (020) orientations [33].

Despite experimental breakthroughs in copper chalcogenide chemistry, the discovery of novel 2D materials is usually time-consuming and expensive. In this respect, crystal structure prediction (CSP) searches emerge as an efficient approach to accelerate the discovery and design of 2D materials [35,36]. To extend the 2D CuX-based structure family, we performed extensive structural searches of 2D CuX by employing an evolutionary algorithm (EA) in combination with DFT calculations.

In this paper, we report the discovery of six phases of 2D CuX materials ( $X=S, Se, Te$ ) from only the knowledge of their chemical composition. These phases are named 2D CuS- $P4/mmm$ , CuS- $P4/nmm$ , CuS- $Pmmn$ , CuSe- $P4/mmm$ , CuSe- $Pmmn$ , and CuTe- $P4/nmm$ . We investigated their viability [37] by the DFT study of their thermodynamic, dynamical, and thermal stabilities of 12 2D CuX structures within  $P\bar{3}m1$ ,  $P4/nmm$ ,  $P4/mmm$ , and  $Pmmn$  space groups as well as their bonding and electronic properties.

The present paper is organized as follows. Section II provides information on the employed computational tools and the methods such as the configurational search approach, DFT calculations, and the main criteria for establishing the stability of the proposed 2D structures. The 2D EA crystal structure search results are discussed in Sec. III A. The energetic and thermal stabilities of the four selected 2D CuX phases are discussed in Sec. III B. The chemical bonding and electronic properties are described in Sec. III C. Our conclusion and final remarks are provided in the last section.

## II. METHODS AND COMPUTATIONAL DETAILS

### A. Crystal structure prediction searches

Configurational exploration methods based on computation enable prescreening for 2D materials by rapidly and accurately identifying 2D material candidates. In this paper, we first examined the energy landscape of each 2D CuX ( $X=S, Se, Te$ ) compound by a series of searches using a fixed-composition EA as implemented in the UNIVERSAL STRUCTURE PREDICTOR: EVOLUTIONARY XTALLOGRAPHY (USPEX) software [38–40]. We used an EA specifically designed in the USPEX code for 2D CSP. During the CSP search, the geometry optimization and total energy calculations of a 2D crystalline structure are carried out using DFT as implemented in the VIENNA AB INITIO SIMULATION PACKAGE (VASP version 5.4.4) [41,42]. The first-principles methodology is described in the next section (Sec. II B). Primitive cells containing up to eight atoms are considered. In the first iteration of USPEX (i.e., the first EA generation), we chose a large number of 80 structures to be generated randomly. All subsequent generations contain at least 60 structures produced from the previous generation, using evolutionary variation operators defined in Refs. [38–40]. A ratio of 50%, 30%, and 20% is chosen for the generation of these 60 structures using heredity, random planar symmetry, and transmutation

(of Cu and X atoms), respectively. In 3D space, layers of 2D materials are separated by a vacuum thickness of 15 Å to avoid interlayer interactions. In USPEX calculations, five successive steps of increasing accuracy are employed to improve the geometry convergence. The *ab initio* methodology corresponding to the latest step is described in Sec. II B. Then, all 2D CuX structures within 200 meV/atom of the convex hull (formed by the structure with the most favorable total energy) are considered as possible thermodynamic (meta)stable phases. The geometrical and electronic properties of them are investigated in the following.

### B. DFT methodology

The first-principles calculations were performed using a projected-augmented-wave (PAW) [43] method as implemented in the VASP package. The Perdew-Burke-Ernzerhof (PBE) [44] exchange-correlation functional was used within the generalized gradient approximation (GGA) [45]. A cutoff energy of 520 eV was used for all the systems. All the 2D structures were optimized until the net forces on the atoms were below 1 meV/Å and the total stress tensor deviated by  $\leq 0.01$  GPa, resulting in enthalpies that converged to less than 1 meV/atom (lower than a chemical accuracy of 1 kcal/mol, i.e., 0.04 eV/atom). The Brillouin zone was sampled using a  $\Gamma$ -centered, uniform  $k$ -point grid with a resolution of  $2\pi \times 0.04 \text{ \AA}^{-1}$  for all selected structures. All EA searches are done at the PBE level of theory: the enthalpy at zero Kelvin is computed at the same PBE-level methodology that was used to optimize the crystal structure. For the energetic aspect, the strongly constrained and appropriately normed (SCAN) meta-GGA functional [46] is also used. Finally, to determine the electronic properties, the Heyd-Scuseria-Ernzerhof (HSE06) functional [47] was used on the PBE-level optimized structure and referred to as HSE06//PBE. Because  $d$  splitting is sensitive to the quantum mechanical methodologies, the electronic structures of all predicted 2D CuX were also obtained by using the Hubbard model, i.e., PBE+U [48,49] and employing  $U = 4$  eV. Furthermore, the magnetism was checked to determine the preferred magnetic ground for our 2D CuX, as presented in Table S2 of the Supplemental Material (SM) [50]. All 2D CuX phases are nonmagnetic, therefore, spin polarization was not taken into account in this paper.

### C. Criteria of stability

In performing a CSP search for novel materials, an essential aspect is to judge the stability of the predicted phases. For this purpose, three main criteria have been used in our paper to examine the dynamical, thermodynamical, and thermal stability of our 2D CuX candidates.

We assert the structure as dynamically stable by the absence of imaginary frequencies in the phonon dispersion diagram. The structure then corresponds to a local enthalpy minimum, i.e., a stable or metastable crystalline solid. Real-space force constants were calculated using the density functional perturbation theory [51] as implemented in the VASP package, which relies on finite displacements. The calculations were done on supercells of the PBE-optimized

structure candidates and phonon frequencies were calculated from the force constants using the PHONOPY [52] code.

The thermodynamic stability of a 2D  $\text{CuX}$  structure was examined by calculating its enthalpy of formation and cohesive energy. The former was given at zero Kelvin as  $\Delta H_f = H_{\text{CuX}} - (H_{\text{Cu}} + H_X)$ . The enthalpy  $H$  was obtained by  $H = E_e + PV$ , with  $E_e$ ,  $P$ , and  $V$ , the total electronic energy, external pressure, and structure cell volume, respectively. The bulk of Cu ( $Fm\bar{3}m$ ), S ( $P2_1/c$ ), Se ( $P2_1/c$ ), and Te ( $P3_121$ ) were taken as references for the calculation of  $H_{\text{Cu}}$ ,  $H_S$ ,  $H_{\text{Se}}$ , and  $H_{\text{Te}}$ , respectively.

The effect of the zero point energy (ZPE) on the stability of bulk and 2D  $\text{CuX}$  compounds was also studied. Its inclusion only slightly modified the enthalpies of formation and the cohesive energies. Therefore, the energies presented in this paper are not ZPE corrected.

Besides the dynamical stability criterion, we investigated the thermal stability of each proposed  $\text{CuX}$  structure at different temperatures by performing *ab initio* molecular dynamic (AIMD) simulations. The chosen 2D supercells are of  $2 \times 2 \times 1$  or  $3 \times 3 \times 1$  sizes, with number of atoms up to 128. These AIMD calculations were carried out in canonical ensemble with a fixed number of atoms ( $N$ ), system's volume ( $V$ ), and temperature ( $T$ ) by employing the Nose-Hoover thermostat. The initial temperature was set at 1000 K, then if the 2D  $\text{CuX}$  structure decomposes, a second AIMD simulation was performed at 800 K, and so on at 600, 400 K, and finally at 300 K. The AIMD simulation time is 10 ps in total with a time step of 2 fs. The VASP software using the previously described PBE functional within GGA was used, while the Brillouin zone integration was reduced to the  $\Gamma$  point of the supercells, owing to the high computational cost of the AIMD simulations.

#### D. Bonding and electronic properties analysis

To perform chemical bonding analysis, we obtained band structures, total and projected density of states (DOS), and electron localization function (ELF) from the optimized PBE geometries obtained by VASP. Additionally, the crystal overlap Hamilton population was calculated using the LOBSTER [53] package. The bond orders (BOs) were computed by the CHARGEMOL program [54] using Manz's BO equation [55] with density derived electrostatic and chemical (DDEC6) partitioning [54,56]. The charge analyses were performed by employing the Bader charge analysis program of Henkelman *et al.* [57]. Finally, the GDIS visualization software [58] which interfaced the USPEX and VASP codes was employed. In this paper, images of the structures are produced using VESTA [59] software.

### III. RESULTS AND DISCUSSION

#### A. In silico prediction of copper chalcogenides phases

We performed extensive CSP searches of 2D  $\text{CuX}$  ( $X=\text{S}$ ,  $\text{Se}$ ,  $\text{Te}$ ) as explained in Sec. II A. For each copper chalcogenide system, more than 800 structures were generated per USPEX run. These structures define a potential energy surface (PES) on which we select all low-lying energetic 2D  $\text{CuX}$  structures within a 200 meV/atom energy window (see Fig.

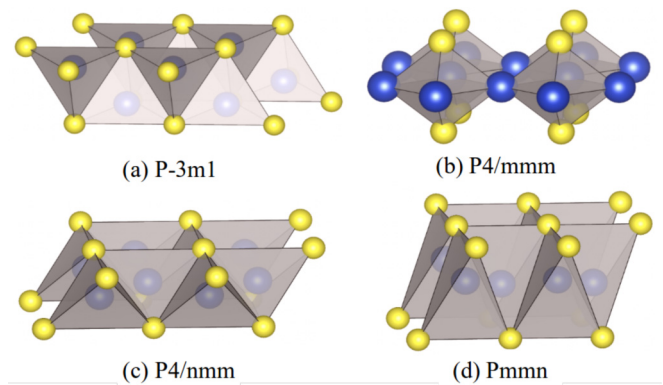


FIG. 1. Views of the four single  $\text{Cu}_2\text{X}_2$  sheets of 2D  $\text{CuX}$  phases, (a)  $P\bar{3}m1$ , (b)  $P4/mmm$ , (c)  $P4/nmm$ , and (d)  $Pmnm$ . Their copper-chalcogen coordination polyhedra are enlightened. Cu and X ( $X=\text{S}$ ,  $\text{Se}$ ,  $\text{Te}$ ) atoms are shown in blue and yellow, respectively.

S1 of the SM [50] which illustrates some of these geometries). Following this criterion and phonon calculations, four stationary points are localized on the PES that correspond to hexagonal  $P\bar{3}m1$ , square  $P4/mmm$ , and  $P4/nmm$ , and orthorhombic (centered rectangular)  $Pmnm$  Bravais lattices. Their 2D crystal structures are displayed in Fig. 1 and their bonding is discussed in Sec. III C. In the following, we discuss general structural aspects of these four geometries.

The hexagonal  $P\bar{3}m1$  slab presents the structural arrangement found in the anionic sublattice of the  $\text{CaAl}_2\text{Si}_2$  structure type while the square  $P4/nmm$  structure is isostructural to the  $\text{Cr}_2\text{Si}_2$  layers found in  $\text{ThCr}_2\text{Si}_2$  structure type. In both  $P\bar{3}m1$  and  $P4/nmm$  structures, the Cu atom resides at the center of an  $X_4$  tetrahedron, and these tetrahedra pack differently to form the aforementioned types of 2D crystals. In  $P\bar{3}m1$ , each tetrahedron shares three of its six edges, while in  $P4/nmm$  it shares four edges.

The third structure of 2D  $\text{CuX}$ ,  $P4/mmm$ , also has a square lattice.  $P4/mmm$  and  $P4/nmm$  slabs have both square copper and chalcogen lattices. These compounds differ from the packing of their two chalcogen monolayers, i.e., an AA packing is observed in  $P4/mmm$  with  $\text{Cu}_4\text{X}_2$  square bipyramidal units sharing four Cu-Cu edges while an AB packing is present in  $P4/nmm$ .

Finally, the fourth and last crystal structure type of 2D  $\text{CuX}$  has a centered rectangular lattice with a  $Pmnm$  space group. The  $\text{Cu}_2\text{X}_2$  slab may be viewed as a compressed  $P4/nmm$  structure along one lattice direction, leading to  $\text{Cu}_4$  rhombi with square tilings. Here, a  $X_4$  square net transforms into a  $X_4$  rectangular network from  $P4/nmm$  to  $Pmnm$  2D structures, and the copper lattice is slightly corrugated in  $Pmnm$  phase.

All  $P\bar{3}m1$ ,  $P4/nmm$  and  $Pmnm$  phases have  $\text{CuX}_4$  tetrahedra (elongated in  $Pmnm$ ), while  $P4/mmm$  presents  $\text{CuX}_4$  square planar units. Finally, while  $P\bar{3}m1$  presents three-coordinated Cu centers in its metal sublattice (nearest Cu atoms), the other 2D structures have four-coordinated Cu centers. All chalcogen atoms are connected to the four nearest Cu neighbors. We will describe the calculated structural parameters in more detail further in Sec. III C.

We note that these four  $\text{CuX}$  slabs present a different energy ranking depending on the chalcogen element X (see Fig. 2),

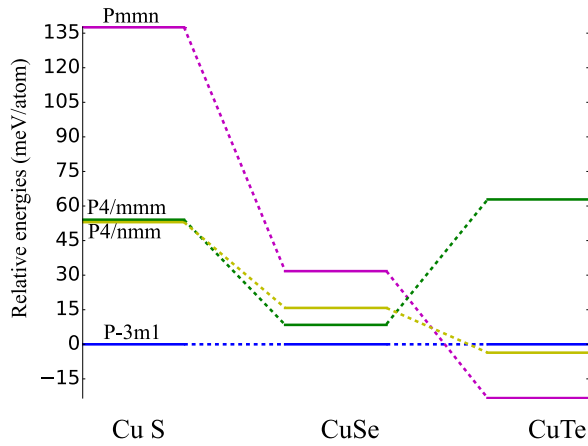


FIG. 2. Total energies (in meV/atom, PBE level) of the four lowest structures of CuS, CuSe, and CuTe compounds, relative to the  $P\bar{3}m1$  phase. (The dotted lines between each chalcogenide structure with the same geometry is just a guide for the eye.)

and a dedicated discussion will follow in Sec. III B. We confirmed that these 12 stationary points are local minima, owing to their dynamical stability. This is shown by the absence of imaginary frequencies in their phonon dispersion curves (see Fig. S2 of the SM [50]).

Our EA-DFT searches lead to the discovery of unique 2D copper chalcogenide materials, namely,  $P4/mmm$  CuX phases ( $X=S, Se, Te$ ), CuS  $P4/nmm$ , and CuSe  $Pmmm$ . While other found structures have been previously proposed, i.e., CuS  $P\bar{3}m1$  and  $Pmmm$ , CuSe  $P\bar{3}m1$  and  $P4/nmm$ , and CuTe  $P\bar{3}m1$ ,  $P4/nmm$ , and  $Pmmm$ , no detailed study of the dynamic, thermodynamic, and thermal stabilities was reported. It is therefore the topic of the next sections: the study of energetic, structural, thermal, bonding, and electronic aspects of the 12 phases of 2D copper chalcogenides discovered by our CSP search.

### B. Energetic and thermal stabilities

The total PBE energies relative to the  $P\bar{3}m1$  structure is plotted in Fig. 2 for each 2D CuX system. The order of stability of the four structures is roughly identical in both CuS and CuSe systems,  $P\bar{3}m1$  being the ground-state 2D structure. The  $P4/mmm$  and  $P4/nmm$  phases are in a quasidegenerate energy state (within our minimization accuracy), for CuS, while the difference is more pronounced but still low (8 meV/atom) for the corresponding phases of CuSe. Nevertheless, a rough estimation of activation energy from  $P4/nmm$  to  $P4/mmm$  which was obtained via step by step and concerted models (Fig. S8 of the SM [50]) shows that the associated activation barrier is high in energy (Fig. S9 of the SM [50]): 1.40, 1.31, and 2.18 eV for CuS, CuSe, and CuTe, respectively. This should prevent the transition between  $P4/mmm$  and  $P4/nmm$  at moderate temperatures (details are given in Sec. S6 of the SM [50]). It also means that, while close in energy, the  $P4/mmm$  and  $P4/nmm$  polymorphs may be synthesized from different precursors and/or experimental procedures. Conversely, the 2D CuTe exhibits a ground-state structure in the  $Pmmm$  geometry. It is noteworthy that the ground state phase of the 3D solid-state CuTe (bulk phase)

TABLE I. Formation enthalpies (in meV/atom) of the predicted 2D CuS, CuSe, and CuTe structures at the PBE level of theory. Boldface entries emphasize the lowest energy phases.

Structure (space group)	2D CuS	2D CuSe	2D CuTe
$P\bar{3}m1$	<b>-82</b>	<b>-75</b>	-46
$P4/mmm$	-28	-67	+17
$P4/nmm$	-29	-59	-50
$Pmmm$	+56	-43	<b>-69</b>

presents a layered structure where our proposed 2D- $Pmmm$  CuTe slabs are stacked in a similar AA stacking configuration. Our *ab initio* CSP search thus leads to the experimentally characterized CuTe layer topology, assuming only the CuTe chemical formula.

The enthalpies of formation of the 12 2D CuX phases are given in Table I. Excluding CuS  $Pmmm$  and CuTe  $P4/mmm$ , the formation enthalpies are negative, indicating the thermodynamic stability of the structures. These computed  $\Delta H_f$  at the PBE level fall into the calculated formation enthalpy range of experimentally characterized known 2D materials [60]. This result allows us to invite the experimental materials community to investigate our predicted 2D CuX compounds. In addition, the formation enthalpies ( $\Delta H_f$ ) of dynamically stable 2D CuX phases and reported 2D materials were calculated as summarized in Table S3 of the SM [50]. Notably, the synthesized  $P\bar{6}m2$  [29,30] CuSe is predicted in our USPEX searches, with formation enthalpy of 0.160 eV/atom, which is relatively higher than the CuSe phases reported in our paper. Moreover, considering supported 2D compounds CuSe ( $\Delta H_f = 0.160$  eV/atom),  $\text{Cu}_2\text{Si}$  [61,62] ( $\Delta H_f = 0.413$  eV/atom), and SiC [63] ( $\Delta H_f = 0.293$  eV/atom) have been synthesized and characterized, we hope our theoretical findings will stress the interest of experimental colleagues and lead to the experimental realization of 2D CuX on proper surfaces.

Besides the PBE GGA, the SCAN meta-GGA and hybrid HSE06 functionals have been employed to evaluate the relative stability of the 2D CuX structures. The 2D structures were fully optimized at the SCAN level of theory while single point energy HSE06 calculations are undertaken at the PBE geometry (HSE06//PBE level). Table II compiled the results obtained from each functional. To simplify the comparison of values, the total energies are reported relative to the  $P\bar{3}m1$  structure of each copper chalcogenide.

For the 2D CuS structures, the stability order is not changed by the different functionals. For 2D copper selenide phases, the energy difference between the two lowest structures tends to be null when SCAN and HSE06//PBE levels are considered;  $P4/mmm$  2D CuSe becomes almost isoenergetic to  $P\bar{3}m1$  2D CuSe. Therefore, one might conclude that both  $P4/mmm$  and  $P\bar{3}m1$  2D CuSe structures are potential synthesizable phases.  $Pmmm$  CuTe phase is the lowest energetic structure at all levels of theory, but we note that  $P4/nmm$  is located at only 2–5 meV/atom above  $Pmmm$  at SCAN and HSE06 levels of theory. Finally, the order for the third and fourth least stable 2D structures is not changed regardless of our level of theory.

TABLE II. Total energy per atom relative to the  $P\bar{3}m1$  structure (in meV/atom) of the 2D CuX structures at PBE, SCAN, and HSE06 levels of theory.<sup>a</sup> Boldface entries emphasize the lowest energy structures.

Compound	Structure	PBE	SCAN	HSE06//PBE
CuS	$P\bar{3}m1$	<b>0</b>	<b>0</b>	<b>0</b>
	$P4/mmm$	54	41	39
	$P4/nmm$	53	93	76
	$Pmnn$	138	98	160
CuSe	$P\bar{3}m1$	<b>0</b>	<b>0</b>	<b>0</b>
	$P4/mmm$	8	<b>-1</b>	<b>-2</b>
	$P4/nmm$	16	52	40
	$Pmnn$	32	72	64
CuTe	$P\bar{3}m1$	0	0	0
	$P4/mmm$	63	94	63
	$P4/nmm$	-4	-8	-9
	$Pmnn$	<b>-23</b>	<b>-13</b>	<b>-11</b>

<sup>a</sup>All the energies were obtained by doing a full geometry optimization, except for the HSE06 functional for which a single point calculation is performed on the optimized PBE structure, named HSE06//PBE.

The thermal stability of the structures was investigated via AIMD simulations at different temperatures. The calculated temperatures at which a structure remains stable, i.e., does not decompose, are summarized in Table III. Snapshots of the structures in the end of the 10 ps AIMD simulations are shown in Figs. S3–S5 of the SM [50].

According to AIMD results, the most thermally stable structure for 2D CuS has the  $P\bar{3}m1$  geometry. This structure is found stable up to 800 K. The  $P4/nmm$  and  $P4/mmm$  structures are thermally stable up to 600 and 400 K, respectively. The simulations of  $Pmnn$  showed that the structure is not stable even at 300 K.

The results of AIMD simulations for 2D CuSe show that the structures with  $P\bar{3}m1$  and  $P4/mmm$  symmetry are the most stable structures with a stability temperature up to 600 K. The other two phases are not so stable:  $Pmnn$  is found stable at 300 K only and  $P4/nmm$  is not stable at this temperature.

Finally, for 2D CuTe structures, the  $P\bar{3}m1$  geometry is found to be the most stable, with a stability temperature up to 800 K. Interestingly, the most energetically favorable geometry,  $Pmnn$ , is not the most thermally stable one, which means that the activation barrier for decomposition is lower

TABLE III. Calculated temperatures (in K) at which the predicted 2D CuX ( $X = S, Se, Te$ ) structures were found thermally stable in the temperature range of 300–1000 K. Boldface entries emphasize the lowest energy phases.

	CuS	CuSe	CuTe
$P\bar{3}m1$	<b>800</b>	<b>600</b>	800
$P4/mmm$	400	600	<sup>a</sup>
$P4/nmm$	600	<sup>a</sup>	300
$Pmnn$	<sup>a</sup>	300	<b>600</b>

<sup>a</sup>At 300K, our AIMD simulation leads to the breaking of Cu–X bonds.

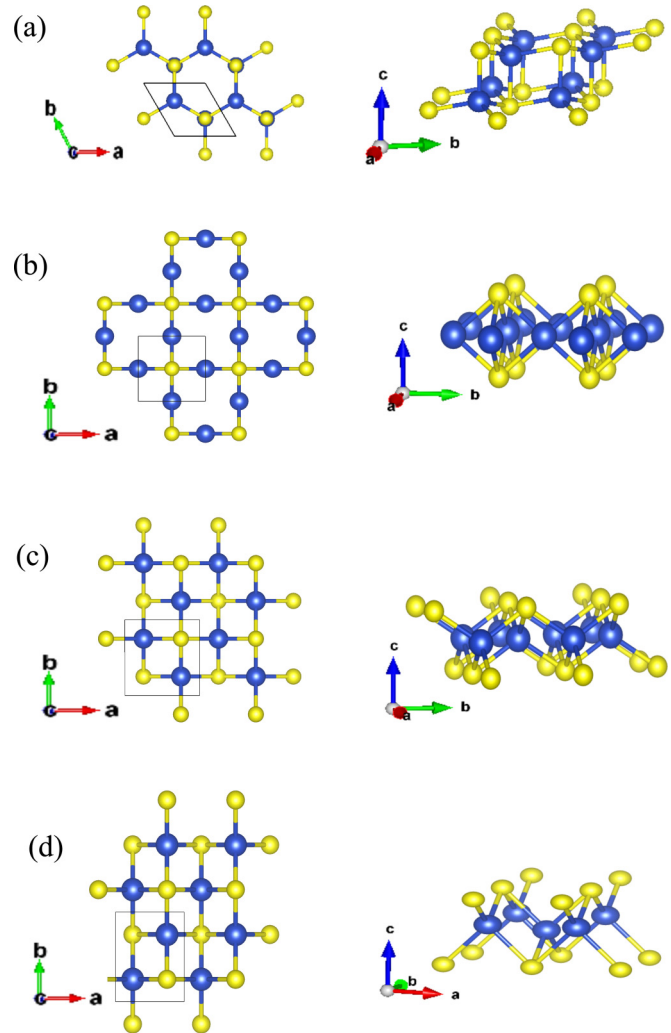


FIG. 3. Extended top and side views of the (a)  $P\bar{3}m1$ , (b)  $P4/mmm$ , (c)  $P4/nmm$ , and (d)  $Pmnn$  structures. The primitive cell of each structure is shown in solid line. Cu and chalcogen ( $X = S, Se, Te$ ) atoms are shown in blue and yellow, respectively. The  $c$  axis is perpendicular to the  $Cu_2X_2$  slab.

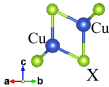
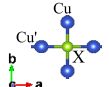
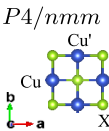
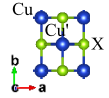
for  $Pmnn$ . This result shows the importance of kinetic criteria in the prediction of viable compounds.

### C. Structural, bonding, and electronic properties of $Cu_2X_2$ slabs

As discussed previously, 2D CuX compounds present four low-lying structure types. Different views of their associated  $Cu_2X_2$  slabs are depicted in Figs. 1 and 3. In the following, we provide a more detailed structural description for each geometry, and discuss their chemical bonding mode. Both Manz’s BO and integrated crystal overlap Hamilton population (ICOHP) are computed. We found that both analyses give the same conclusion. Thus, only the ICOHP descriptor of bond strength will be discussed thereafter. It is presented in Table IV (see Fig. S10 of the SM [50] for BO results).

The first structure shown in Fig. 3(a) crystallizes in a trigonal system with the  $P\bar{3}m1$  space group (No. 164,  $Z = 2$ ). This slab is constructed from two parallel layers of X chalcogen atoms arranged in monolayer triangular lattices. The Cu atoms

TABLE IV. Bond length  $l$  (in Å) and integrated crystal Hamilton population (ICOHP in eV/pair) in  $\text{CuX}$  ( $X = \text{S, Se, Te}$ ) 2D structures.  $\text{Cu}'(X')$  denotes a second type of Cu ( $X$ ) atom considered for BO calculation.

structure	bond	CuS		CuSe		CuTe	
		$l$	ICOHP	$l$	ICOHP	$l$	ICOHP
 $P3m1$	Cu-Cu'	2.87	0.10	2.61	0.25	2.61	0.26
	Cu-X	2.26	1.69	2.41	1.57	2.61	1.31
	Cu'-X	2.36	1.19	2.50	1.40	2.63	1.42
	X-X	3.63	0.19	3.76	0.18	3.90	0.22
 $P4/mmm$	Cu-Cu'	2.56	0.21	2.64	0.22	2.76	0.18
	Cu-X	2.34	1.39	2.46	1.42	2.63	1.30
	X-X <sup>a</sup>	2.95	0.40	3.21	0.52	3.51	0.46
	X-X <sup>b</sup>	3.62	0.03	3.73	0.08	3.91	0.11
 $P4/nmm$	Cu-Cu'	2.74	0.11	2.62	0.20	2.62	0.23
	Cu-X	2.30	1.49	2.45	1.48	2.64	1.24
	X-X	3.70	0.17	3.71	0.19	3.70	0.33
 $Pmnm$	Cu-Cu'	2.58	0.19	2.57	0.26	2.66	0.24
	Cu-X	2.29	1.57	2.42	1.57	2.62	1.37
	Cu'-X	2.45	0.93	2.59	0.88	2.73	0.88
	X-X <sup>c</sup>	2.97	0.53	3.09	0.69	3.26	0.89
	X-X <sup>d</sup>	3.99	0.15	3.90	0.15	4.05	0.16

<sup>a</sup>Between monolayers,

<sup>b</sup>in-plane,

<sup>c</sup>short,

<sup>d</sup>long.

similarly resemble two parallel triangular monolayers, sandwiched between the two  $X$  monolayers. In other words, the combination of each  $X$  monolayer with its adjacent Cu layer makes a buckled honeycomb  $\text{Cu}_2\text{X}_2$  lattice. Each Cu atom is then bonded to four equivalent  $X$  atoms to form a mixture of edge and corner-sharing  $\text{CuX}_4$  tetrahedra [see Fig. 1(a)]. The interatomic distances between Cu– $X$  and Cu–Cu atoms are also given in Table IV. The average bond length of Cu– $X$  for this geometry is 2.31, 2.46, and 2.62 Å in CuS, CuSe, and CuTe, respectively. The size of the tetrahedra, therefore, increases with the atomic number. Conversely, Cu–Cu separation decreases significantly when selenium or tellurium atoms substitute sulfur ones in  $P3m1$  slab, a factor that can explain the relative energetic destabilisation of this phase in going from S to Se to Te in respect to the three other dynamically stable structures.

The second structure  $P4/mmm$   $\text{Cu}_2\text{X}_2$  slab, shown in Figs. 1(b) and 3(b), is formed by a square lattice of copper atoms with capping chalcogen atoms sitting in the apical positions of square bipyramids. Here, each Cu atom is then bonded in a square coplanar geometry to four  $X$  atoms. The Cu– $X$  bond lengths are 2.34, 2.46, and 2.63 Å for CuS, CuSe, and CuTe, respectively, increasing with the atomic number. Contrary to the  $P3m1$  geometry, the same behavior is also observed for  $d_{\text{Cu–Cu}}$ , an increase from 2.56 Å to 2.76 Å in going from S to Te (see Table IV). In 2D  $P4/mmm$  CuTe, a short Te–Te separation of 3.51 Å is observed.

The third structure  $P4/nmm$  also possesses a square lattice of Cu atoms. As can be seen in Fig. 3(c), the  $P4/nmm$  phase (No. 129,  $Z = 2$ ) can be regarded as a structural modification of the  $P4/mmm$  slab. From  $P4/mmm$  to  $P4/nmm$ , one chalcogen

atom is migrating from its fourfold position to be located under a chalcogen atom making the square bipyramidal  $\text{Cu}_4\text{X}_2$  unit. Thus,  $P4/nmm$   $\text{Cu}_2\text{X}_2$  slab is then constructed from three nonequivalent square monolayers with AB stacking.  $\text{Cu}_4\text{X}_2$  square bipyramids share their four basal Cu–Cu edges in this extended 2D  $\text{Cu}_2\text{X}_2$  net. The Cu– $X$  bond lengths are similar to the ones found in  $P4/mmm$ , showing the weak effect of the chalcogen position on the Cu $X$  bond lengths. Conversely, Cu–Cu distances decrease in  $\text{Cu}_2\text{X}_2$  slabs from S (2.74 Å) to Se (2.62 Å) then remain constant from Se to Te (2.62 Å). This structural behavior may explain the energetic stabilisation of  $P4/nmm$  when going from S to Te.

Finally, our fourth Cu $X$  candidate crystallizes in a rectangular 2D system and has the orthorhombic  $Pmnm$  space group (No. 59,  $Z = 2$ ). Its topology resembles that of the  $P4/nmm$  structure with rectangular  $\text{Cu}_4$  units rather than square ones [see Fig. 1(d)]. There are two short and two long Cu– $X$  bond lengths, and similarly, short and long  $X$ – $X$  distances. This  $\text{Cu}_2\text{X}_2$  slab is encountered of distorted tetrahedral  $\text{CuX}_4$  units is encountered as the lowest energy ground-state structure in 2D CuTe compound. This net allows short Te–Te separations of 3.26 Å and significant Te–Te bonding is computed [ICOHP(Te–Te) = 0.89].

A question arises: What electronic factors govern the energy ranking of these four 2D geometries? To approach an answer to this question, we need to understand the structural details of these 2D nets. To do so, we have undertaken orbital interaction analysis with the assistance of total and projected DOS, ICOHP, and BO calculations. We refer to the seminal work of Zheng and Hoffmann [64] on the bonding in the  $\text{ThCr}_2\text{Si}_2$  and  $\text{CaAl}_2\text{Si}_2$  structures. These prototypes contain

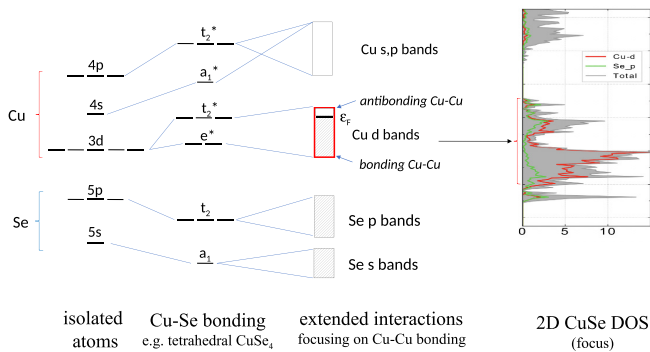


FIG. 4. (a) Construction of the two-dimensional bands in 2D CuSe; (b) calculated total and projected density of states for 2D CuSe  $P\bar{3}m1$ .

2D  $M_2X_2$  lattices related to the ones found in our predicted 2D CuX networks. A schematic construction of the CuX two-dimensional bands is presented in Fig. 4 (Se is taken as an example), starting from the separate Cu and Se atoms (valence orbitals), building the  $CuX_4$  molecular units, then generating the extended 2D net. We start with a simplified molecular orbital diagram of a  $CuX_4$  molecular unit, displayed in Fig. 4. Here, we choose a tetrahedral geometry for  $CuX_4$  as observed in  $P\bar{3}m1$  and  $P4/nmm$ , but the elongated tetrahedral ( $Pnmm$ ) or square planar ( $P4/nmm$ ) geometries of  $CuX_4$  will lead to the same general bonding picture.

The metal Cu  $d$  orbitals split into  $e$  and  $t_2$  sets, and these (slightly) antibonding metal-ligand molecular levels develop into Cu  $d$  bands when going to the extended 2D CuSe net. This simplified orbital model is confirmed by the calculated DOS displayed in Fig. S6 of the SM [50]. Note that the dispersion of the  $d$  bands is related to the coordination of copper atoms: the  $d$  band is larger in the four-coordinate Cu lattice, i.e.,  $P4/nmm$ ,  $P4/mmm$ , and  $Pmnm$ , than in three-coordinate one,  $P\bar{3}m1$ . The bottom of the  $d$  band block is Cu–Cu bonding and the top Cu–Cu antibonding and, because of the overlap, the antibonding contribution is stronger than the bonding—a phenomenon encountered in the four-electron two-orbital repulsion. In the extended CuSe net, the Fermi level crosses a high DOS, as expected for a  $d^9$  metal. From the DOS and band structure calculations analysis at the PBE and PBE+U levels, all 2D compounds are metallic (see Fig. S6 of the SM [50]). So, all the structures are still metal and their band structures present globally the same trends.

Let us focus now on  $P\bar{3}m1$  and  $P4/nmm$  structures, as representative nets with three- and four-coordinate copper atoms, respectively. One may see from Table IV that  $P\bar{3}m1$   $Cu_2X_2$  slab presents among the four proposed 2D structures with the strongest copper-chalcogen Cu–X ICOHP. This result validates the Zheng and Hoffmann orbital interaction model [64]: in a less dispersive metal sublattice, i.e., in  $P\bar{3}m1$  three-coordinate Cu lattice, the metals interact better with the ligand sublattice. This criterion alone cannot, however, explain the relative stability of the four predicted 2D CuX nets; other subtle electronic effects must be involved.

The  $P\bar{3}m1$  structure has a corrugated Cu net where each metal is coordinated to three others, while the bare metal layer in  $P4/nmm$  (as well as  $P4/mmm$ ) is then a square lattice with four coordinated metal atoms. Thus, the copper  $d$  band

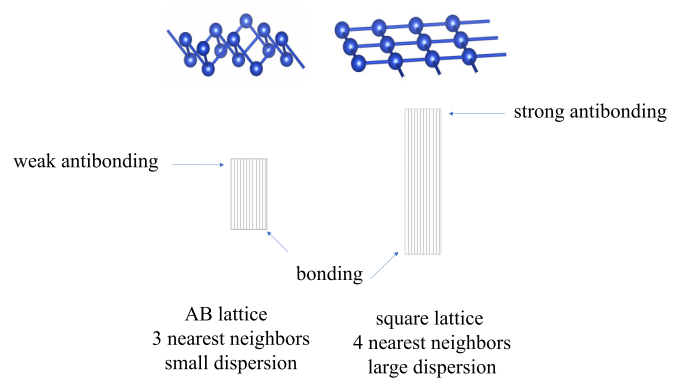


FIG. 5. Copper  $d$  band dispersion in corrugated and planer Cu net with three-coordinated Cu lattice  $P\bar{3}m1$  and four-coordinated one  $P4/nmm$ , respectively.

dispersion is smaller in three-coordinate Cu lattice  $P\bar{3}m1$  than in four-coordinate one  $P4/nmm$ , as schematically illustrated in Fig. 5. This band is also Cu–X antibonding (more at the top of the band). Bonding and antibonding Cu–Cu orbital overlaps are weaker at the bottom and the top of the  $d$  band in  $P\bar{3}m1$ . Therefore, for a high band filling,  $d^9$   $Cu^{2+}$  in CuX, three-coordinate Cu  $P\bar{3}m1$  should be then energetically favored while four-coordinate Cu structures are more destabilized. This is what we observed in 2D CuS. Sulfur is the most electronegative element in the chalcogen family, while Te is the least one (2.58, 2.55, and 2.10 on the Pauling scale for S, Se, and Te, respectively). Thus, in 2D CuS, one may safely assign a formal +2 charge for Cu, i.e.,  $d^9$  configuration, and the octet is obeyed for  $S^{2-}$ . As calculated at all levels of theory, the  $P\bar{3}m1$   $Cu_2S_2$  slab is by far the most stable structure while the other structures with four-coordinated metals are located higher in energy.

By replacing S by Se, the Cu–X electronegativity difference is lowered, thus the Cu–X charge transfer decreases. One may expect a formal  $d^n$  configuration of copper higher than  $d^9$ . When the  $d$  band is completely filled, three-coordinate Cu and four-coordinate Cu slabs must compete in energy. This crude model explains well why  $P\bar{3}m1$  and  $P4/mmm$  are closer in energy in 2D CuSe. Now, why is  $P4/mmm$  with  $Cu_4Se_2$  square bipyramidal units lower in energy than  $P4/nmm$  with  $Cu_4Se$  square pyramidal units? In  $P4/mmm$ , the computed Se–Se ICOHP is larger in  $P4/mmm$  than in  $P4/nmm$  (0.52 versus 0.19, respectively) because of the through-space Se–Se stabilizing interaction present in  $Cu_4Se_2$  units. A short interlayer Se–Se separation of 3.21 Å is observed in the  $P4/mmm$   $Cu_2Se_2$  slab, reflecting the delocalization of electrons over the whole cluster.

Finally, Te is the less electronegative element of this chalcogen trio, with the biggest element radius. This chemical composition adopts the  $Pmnm$  geometry as its lowest energy structure at PBE level. A corrugated copper monolayer is observed in response to the packing of Te atoms. Each copper atom seats in an elongated  $Te_4$  tetrahedron with small and large Te–Cu–Te bond angles ( $73.4^\circ$  and  $101.4^\circ$ ). This structural arrangement leads to short (3.26 Å) and long (4.05 Å) in-plane Te–Te bond lengths. Thus, a significant Te–Te bonding is calculated along each 1D tellurium chain with a

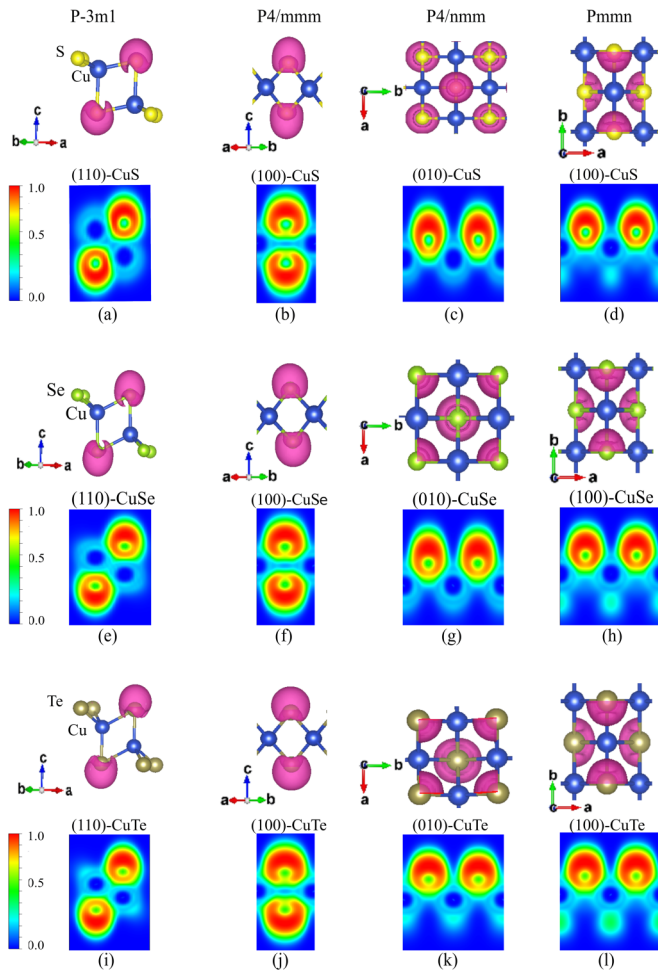


FIG. 6. 3D and 2D electron localization function (ELF) of CuX compounds in  $P\bar{3}m1$ ,  $P4/mmm$ ,  $P4/nmm$ , and  $Pmmn$  structures. Both 3D and 2D plots are given for an ELF value of 0.8.

computed ICOHP(Te–Te) of 0.89 eV/pair (see Table IV). This bonding mode stabilizes this structure type, as in  $P4/mmm$  which is almost isoenergetic to  $Pmmn$  at SCAN and HSE06 levels of theory. In both  $Pmmn$  and  $P4/mmm$  structures, some delocalized Te–Te covalent bonding is observed (see Table IV).

Our ELF analysis shows that electron density is delocalized along the X–X chains in each X monolayer of  $Pmmn$  CuX (see

Fig. 6). Meanwhile, a strongly localized lone pair is observed on each chalcogen atom in the other structures, specifically on electronegative sulfur atoms. This is expected for a six-valence electron atom in such a coordination mode.

#### IV. CONCLUSION

This paper presents a CSP search for 2D copper chalcogenide CuX compounds. The extensive search was carried out by using EA and *ab initio* calculations based on DFT. According to our results, four geometries with space groups  $P\bar{3}m1$ ,  $P4/mmm$ ,  $P4/nmm$ , and  $Pmmn$  are predicted for 2D CuX ( $X=S$ , Se, and Te). All the 2D CuX phases reported in this paper are nonmagnetic. These geometries were confirmed to be dynamically stable. The  $P\bar{3}m1$  geometry has the lowest formation energy for CuS and CuSe 2D materials. Conversely, the  $Pmmn$  geometry is a global minimum for the 2D CuTe structure. Moreover, the thermal stability of the structures was investigated by AIMD simulations at different temperatures. The  $P\bar{3}m1$  structure, which is determined by AIMD studies to be stable up to 800, 600, and 800 K for CuS, CuSe, and CuTe, respectively, is found to be the most thermally stable structure. For CuSe, a structure with the  $P4/mmm$  symmetry is also equivalently stable at the same temperature. Comprehensive chemical bond analyses were done by the investigation of DOS, crystal overlap Hamilton population, ELF, and Manz's BOs. An orbital model is proposed and enlightens the chemical bonding in the 2D nets. The analysis of ICOHP gives insights into the structural stability of 2D CuX nets. All 2D CuX 2D structures have a metallic character with an ionocovalent nature of the Cu–X bonds. We expect that our findings will inspire the materials science community to synthesize our *in silico* proposed two-dimensional CuX phases.

#### ACKNOWLEDGMENTS

We thank the ANR PRCI Predict\_2D\_Nanomats (P.I., G.F.), the FEDER and Nouvelle Aquitaine Region (France). We also acknowledge the High-Performance Computing Centers of Poitiers University (Mésocentre SPIN, France) and the Irene/TGCC, and Jean Zay/IDRIS GENCI (France) under Projects No. X2016087539 and No. A0100807539 for allocation of computing time.

- [1] K. S. Novoselov, A. K. Geim, S. V. Morozov, D. Jiang, Y. Zhang, S. V. Dubonos, I. V. Grigorieva, and A. A. Firsov, *Science* **306**, 666 (2004).
- [2] R. Woods-Robinson, Y. Han, H. Zhang, T. Ablekim, I. Khan, K. A. Persson, and A. Zakutayev, *Chem. Rev.* **120**, 4007 (2020).
- [3] J. H. Han, M. Kwak, Y. Kim, and J. Cheon, *Chem. Rev.* **118**, 6151 (2018).
- [4] X. Zhou and E. E. Rodriguez, *Chem. Mater.* **29**, 5737 (2017).
- [5] A. K. Singh and R. G. Hennig, *Appl. Phys. Lett.* **105**, 042103 (2014).
- [6] C. M. Hessel, V. P. Pattani, M. Rasch, M. G. Panthani, B. Koo, J. W. Tunnell, and B. A. Korgel, *Nano Lett.* **11**, 2560 (2011).
- [7] Y. Zhao and C. Burda, *Energy Environ. Sci.* **5**, 5564 (2012).
- [8] Y. Chen, C. Davoisne, J.-M. Tarascon, and C. Guéry, *J. Mater. Chem.* **22**, 5295 (2012).
- [9] J. Kundu and D. Pradhan, *ACS Appl. Mater. Interfaces* **6**, 1823 (2014).
- [10] A. A. Sagade and R. Sharma, *Sens. Actuators B: Chem.* **133**, 135 (2008).
- [11] Y. Du, Z. Yin, J. Zhu, X. Huang, X.-J. Wu, Z. Zeng, Q. Yan, and H. Zhang, *Nat. Commun.* **3**, 1177 (2012).



- [12] W. Shuang, X. Wang, G. Wang, Y. Guo, K. Wang, G. Yang, L. Zhu, and L. Yang, *J. Mater. Chem. B* **3**, 5603 (2015).
- [13] Y. Huang, Y. Deng, A. D. Handoko, G. K. Goh, and B. S. Yeo, *ChemSusChem* **11**, 320 (2018).
- [14] W. B. Kim, S. H. Lee, M. Cho, and Y. Lee, *Sens. Actuators B: Chem.* **249**, 161 (2017).
- [15] C. Feng, L. Zhang, M. Yang, X. Song, H. Zhao, Z. Jia, K. Sun, and G. Liu, *ACS Appl. Mater. Interfaces* **7**, 15726 (2015).
- [16] Z. Wang, S. Rafai, C. Qiao, J. Jia, Y. Zhu, X. Ma, and C. Cao, *ACS Appl. Mater. Interfaces* **11**, 7046 (2019).
- [17] B. Yu, W. Liu, S. Chen, H. Wang, H. Wang, G. Chen, and Z. Ren, *Nano Energy* **1**, 472 (2012).
- [18] P. Pazhamalai, K. Krishnamoorthy, and S. J. Kim, *Int. J. Hydrogen Energy* **41**, 14830 (2016).
- [19] A. Pashinkin and V. Fedorov, *Inorg. Mater.* **39**, 539 (2003).
- [20] A. Pashinkin and L. Pavlova, *Inorg. Mater.* **41**, 1050 (2005).
- [21] A. Barajas-Aguilar, S. J. Sandoval, and A. M. Garay-Tapia, *J. Phys.: Condens. Matter* **32**, 045403 (2019).
- [22] C. Nethravathi, C. R. Rajamathi, M. Rajamathi, R. Maki, T. Mori, D. Golberg, and Y. Bando, *J. Mater. Chem. A* **2**, 985 (2014).
- [23] B. Mansour, F. Mukhtar, and G. Barakati, *Phys. Status Solidi A* **95**, 703 (1986).
- [24] K. Zhang, X. Liu, H. Zhang, K. Deng, M. Yan, W. Yao, M. Zheng, E. F. Schwier, K. Shimada, J. D. Denlinger, Y. Wu, W. Duan, and S. Zhou, *Phys. Rev. Lett.* **121**, 206402 (2018).
- [25] G. Grüner, *Rev. Mod. Phys.* **60**, 1129 (1988).
- [26] A. L. Soares, Jr., E. C. Dos Santos, A. Morales-García, T. Heine, H. A. De Abreu, and H. A. Duarte, *2D Mater.* **4**, 015041 (2016).
- [27] H. Liang, W. Shuang, Y. Zhang, S. Chao, H. Han, X. Wang, H. Zhang, and L. Yang, *ChemElectroChem* **5**, 494 (2018).
- [28] S. Thirumavalavan, K. Mani, and S. Sagadevan, *Mater. Res.* **18**, 1000 (2015).
- [29] X. Lin, J. Lu, Y. Shao, Y. Zhang, X. Wu, J. Pan, L. Gao, S. Zhu, K. Qian, Y. Zhang *et al.*, *Nat. Mater.* **16**, 717 (2017).
- [30] L. Gao, J.-T. Sun, J.-C. Lu, H. Li, K. Qian, S. Zhang, Y.-Y. Zhang, T. Qian, H. Ding, X. Lin *et al.*, *Adv. Mater.* **30**, 1707055 (2018).
- [31] Y. An, Y. Hou, H. Wang, J. Li, R. Wu, C. Liu, T. Wang, and J. Jiao, *J. Phys.: Condens. Matter* **31**, 355301 (2019).
- [32] F. Golgovici, A.-S. Catrangiu, and T. Visan, *Int. J. Electrochem. Sci.* **11**, 915 (2016).
- [33] Z. Y. Aydın and S. Abacı, *J. Solid State Electrochem.* **21**, 1417 (2017).
- [34] Y. Yang, T. Wang, C. Liu, W. Li, J. Zhang, L. Wu, G. Zeng, W. Wang, and M. Yu, *Vacuum* **142**, 181 (2017).
- [35] H. Şahin, S. Cahangirov, M. Topsakal, E. Bekaroglu, E. Akturk, R. T. Senger, and S. Ciraci, *Phys. Rev. B* **80**, 155453 (2009).
- [36] Y. Ding, Y. Wang, J. Ni, L. Shi, S. Shi, and W. Tang, *Phys. B: Condens. Matter* **406**, 2254 (2011).
- [37] R. Hoffmann, *Am. Sci.* **75**, 619 (1987).
- [38] A. R. Oganov and C. W. Glass, *J. Chem. Phys.* **124**, 244704 (2006).
- [39] A. R. Oganov, A. O. Lyakhov, and M. Valle, *Acc. Chem. Res.* **44**, 227 (2011).
- [40] A. O. Lyakhov, A. R. Oganov, H. T. Stokes, and Q. Zhu, *Comput. Phys. Commun.* **184**, 1172 (2013).
- [41] G. Kresse and J. Hafner, *Phys. Rev. B* **47**, 558 (1993).
- [42] G. Kresse and J. Furthmüller, *Comput. Mater. Sci.* **6**, 15 (1996).
- [43] P. E. Blöchl, *Phys. Rev. B* **50**, 17953 (1994).
- [44] J. P. Perdew, K. Burke, and M. Ernzerhof, *Phys. Rev. Lett.* **80**, 891 (1998).
- [45] J. P. Perdew, K. Burke, and M. Ernzerhof, *Phys. Rev. Lett.* **77**, 3865 (1996).
- [46] J. Sun, A. Ruzsinszky, and J. P. Perdew, *Phys. Rev. Lett.* **115**, 036402 (2015).
- [47] A. V. Krukau, O. A. Vydrov, A. F. Izmaylov, and G. E. Scuseria, *J. Chem. Phys.* **125**, 224106 (2006).
- [48] Y. Zhang, X. Yuan, X. Sun, B.-C. Shih, P. Zhang, and W. Zhang, *Phys. Rev. B* **84**, 075127 (2011).
- [49] Y. Zhang, L. Xi, Y. Wang, J. Zhang, P. Zhang, and W. Zhang, *Comput. Mater. Sci.* **108**, 239 (2015).
- [50] See Supplemental Material at <https://link.aps.org/supplemental/10.1103/PhysRevMaterials.5.124007> for methodological details; calculated structural parameters and energies for all predicted 2D CuX compounds, as well as elements and bulk CuX compounds; phonon dispersion curve; electronic band structure calculations and DOS; COHP; and *ab initio* molecular dynamics simulations of all discussed structures.
- [51] S. Baroni, S. de Gironcoli, A. Dal Corso, and P. Giannozzi, *Rev. Mod. Phys.* **73**, 515 (2001).
- [52] A. Togo and I. Tanaka, *Scr. Mater.* **108**, 1 (2015).
- [53] S. Maintz, V. L. Deringer, A. L. Tchougréeff, and R. Dronskowski, *J. Comput. Chem.* **37**, 1030 (2016).
- [54] N. G. Limas and T. A. Manz, *RSC Adv.* **6**, 45727 (2016).
- [55] T. A. Manz, *RSC Adv.* **7**, 45552 (2017).
- [56] T. A. Manz and N. G. Limas, *RSC Adv.* **6**, 47771 (2016).
- [57] W. Tang, E. Sanville, and G. Henkelman, *J. Phys.: Condens. Matter* **21**, 084204 (2009).
- [58] H. Okadome Valencia, B. Wang, G. Frapper, and A. L. Rohl, *J. Comput. Chem.* **42**, 1602 (2021).
- [59] K. Momma and F. Izumi, *J. Appl. Crystallogr.* **44**, 1272 (2011).
- [60] B. Wang and G. Frapper, *Phys. Rev. Material* **5**, 034003 (2021).
- [61] L.-M. Yang, V. Bacic, I. A. Popov, A. I. Boldyrev, T. Heine, T. Frauenheim, and E. Ganz, *J. Am. Chem. Soc.* **137**, 2757 (2015).
- [62] B. Feng, B. Fu, S. Kasamatsu, S. Ito, P. Cheng, C.-C. Liu, Y. Feng, S. Wu, S. K. Mahatha, P. Sheverdyeva *et al.*, *Nat. Commun.* **8**, 1007 (2017).
- [63] S. Lin, *J. Phys. Chem. C* **116**, 3951 (2012).
- [64] C. Zheng and R. Hoffmann, *J. Solid State Chem.* **72**, 58 (1988).